Materials Advances

ROYAL SOCIETY OF CHEMISTRY

PAPER

View Article Online
View Journal | View Issue

Check for updates

Cite this: *Mater. Adv.*, 2025, 6, 8479

Molecularly imprinted sensor for lipoic acid quantification in serum: a proof-of-concept for diagnosis of NELL-1 membranous nephropathy and kidney failure

Kanwal Bashir,[a] Amir Habib,[b] Imran Shakir,[c] Tajamal Hussain[a] and Adeel Afzal *[a]

Received 18th July 2025,
Accepted 28th September 2025

DOI: 10.1039/d5ma00773a

rsc.li/materials-advances

Sensitive quantification of α-lipoic acid (LA) in human serum is essential for early detection and monitoring of kidney disorders but remains challenging due to interference from complex biological matrices. Here, we report an electrochemical sensor using a molecularly imprinted poly(aniline-*co*-*m*-aminophenol) (MIP) copolymer engineered with porous morphology and low interfacial resistance to enhance charge transfer and selective analyte recognition. Cyclic voltammetry, differential pulse voltammetry, and electrochemical impedance spectroscopy confirm efficient charge transfer, diffusion-controlled kinetics, and a clear analytical response toward LA across 0–500 μM, achieving high sensitivity (2.04 μA cm^{-2} μM^{-1}) and a detection limit of 189 nM. The sensor demonstrates a mean recovery of 102 ± 7.07% in spiked human serum, validating reliable performance under clinically relevant conditions. This work establishes a practical platform for rapid, accurate, and sensitive LA detection, supporting point-of-care diagnostics and continuous monitoring in biomedical applications.

Open Access Article. Published on 29 September 2025. Downloaded on 4/28/2026 6:53:28 PM.
This article is licensed under a Creative Commons Attribution-NonCommercial 3.0 Unported Licence.

1. Introduction

Lipoic acid (LA), an organosulfur compound derived from caprylic acid, plays a critical role in aerobic metabolism and is widely recognized for its potent antioxidant properties. It has been extensively used to treat oxidative stress-related conditions, including diabetic neuropathy and liver ailments.[1] However, while LA is generally considered safe, excessive intake has been associated with adverse effects, most notably nephrotoxicity. Emerging studies have implicated high-dose LA in the development of neural epidermal growth factor-like 1 (NELL-1) associated membranous nephropathy (MN), a kidney disorder marked by immune complex deposition in the glomerular basement membrane, leading to proteinuria, edema, and hypoalbuminemia.[2–5] Given these clinical concerns, regular and precise monitoring of LA concentrations in biological fluids is essential for early diagnosis and ongoing management of related conditions.

Various analytical methods have been developed for LA detection. Spectrophotometric techniques based on complex formation with 3-methyl-2-benzothiazolinone hydrazone (MTBH) or ferric chloride offer relatively simple analysis, with linear detection ranges between 4.0–20.0 μg mL^{-1} at 515 nm.[6] However, such methods suffer from limitations like low sensitivity, poor selectivity, and susceptibility to interference.[7,8] To overcome these drawbacks, chromatographic techniques, such as high-performance liquid chromatography (HPLC),[9] and gas chromatography (GC),[10] have been employed, offering enhanced accuracy and sensitivity. Nevertheless, these methods typically require expensive instrumentation, complex sample preparation, and longer analysis times, limiting their suitability for point-of-care (POC) diagnostics.

In contrast, electrochemical sensors offer a promising alternative due to their low cost, high sensitivity, fast response, and ease of miniaturization.[11–13] Non-enzymatic electrochemical sensors, in particular, have gained attention as they bypass the instability, cost, and storage limitations associated with enzyme-based biosensors. Recent advances in this domain include the use of nanostructured modifiers such as metal oxides and nanoparticles to enhance sensor performance. For example, Charoenkitamorn *et al.*[14] employed MnO_2-modified screen-printed graphene electrodes for the simultaneous detection of coenzyme Q10 and LA, achieving a detection limit of 0.088 μg mL^{-1}. Similarly, Ziyatdinova and Gimadutdinova reported a CeO_2·Fe_2O_3 nanoparticle-modified glassy carbon electrode with a detection limit of 0.053 μM.[15] Gungor *et al.*[16] developed a chitosan–polyurethane membrane-based biosensor with a detection range of 5–200 μmol L^{-1} and a limit of 4.931 μmol L^{-1}.

[a] *Sensors and Diagnostics Lab, School of Chemistry, University of the Punjab, Quaid-i-Azam Campus, Lahore 54590, Pakistan. E-mail: adeel.chem@pu.edu.pk*
[b] *Department of Physics, College of Science, University of Hafr Al Batin, PO Box 1803, Hafr Al Batin 39524, Saudi Arabia*
[c] *Department of Physics, Faculty of Science, Islamic University of Madinah, Madinah 42351, Saudi Arabia*

© 2025 The Author(s). Published by the Royal Society of Chemistry

Open Access Article. Published on 29 September 2025. Downloaded on 4/28/2026 6:53:28 PM.
This article is licensed under a Creative Commons Attribution-NonCommercial 3.0 Unported Licence.

Conducting polymers such as polyaniline (PANI), polypyrrole (PPY), and polythiophene (PTP) have been widely explored for biosensor development due to their excellent electrical conductivity, chemical stability, and biocompatibility.[17–20] Their structural flexibility allows facile functionalization and efficient electron transfer, enhancing biosensor sensitivity.[21] To further improve selectivity, molecular imprinting technology has been introduced. Molecularly imprinted polymers (MIPs) possess highly specific binding cavities complementary in shape and functional groups to the target molecule.[22–24] These biomimetic materials provide enzyme-like selectivity along with superior robustness, reusability, and long-term stability, making them ideal candidates for non-enzymatic electrochemical sensing platforms.[25,26]

Despite these advances, few studies have combined the advantages of conducting polymers and molecular imprinting in a unified sensor system specifically designed for LA detection. To the best of our knowledge, no electrochemical sensor has yet utilized a poly(aniline-*co*-*m*-aminophenol) (PAni–PmAP, or simply referred to as MIP) copolymer matrix, functionalized through molecular imprinting, to detect LA. The use of *m*-aminophenol as a co-monomer introduces hydroxyl functionality into the polymer backbone, enhancing hydrogen bonding and facilitating stronger template interactions during imprinting.

In this study, we report the fabrication and evaluation of a novel molecularly imprinted electrochemical sensor based on PAni–PmAP for the selective and sensitive detection of lipoic acid. The sensor was constructed by coating molecularly imprinted (MIP) and non-imprinted (NIP) polymer films onto screen-printed gold electrodes (SPGEs), enabling low-cost, disposable, and portable sensing. The MIP layer functions as a selective recognition matrix, where the imprinted cavities bind lipoic acid molecules and hinder redox probe diffusion, leading to a measurable decrease in current response as illustrated in Fig. 1. The MIP-based sensor exhibits high sensitivity, reproducibility, and excellent selectivity toward LA in the presence of biologically relevant interferents. This work demonstrates the potential of combining conducting copolymers with molecular imprinting for point-of-care LA diagnostics, aligning with the ASSURED criteria for accessible healthcare technologies.[27]

2. Experimental section

2.1. Synthesis of poly(aniline-*co*-*m*-aminophenol)

Molecularly imprinted poly(aniline-*co*-*m*-aminophenol) copolymer (PAni–PmAP, MIP) was synthesized *via in situ* oxidative polymerization using *m*-aminophenol as the primary monomer, aniline as the co-monomer, α-lipoic acid (LA) as the template, and diphenylamine (DPA) as the cross-linker. Specifically, 80 mg of *m*-aminophenol, 66 μL of aniline, and 248 mg of DPA were dissolved in 10 mL of 0.1 M HCl. The mixture was sonicated for 30 minutes using a 250 W, 450 kHz ultrasonic bath to ensure thorough homogenization. Then, 30 mg of LA was added as the template, followed by another 30 minutes of sonication for uniform dispersion. Separately, an oxidant solution was prepared by dissolving 410 mg of ammonium persulfate (APS) in 10 mL of 0.1 M HCl. This APS solution was added dropwise to the monomer solution under constant stirring at 2000 rpm, initiating the polymerization. The reaction was continued for 4 hours at room temperature

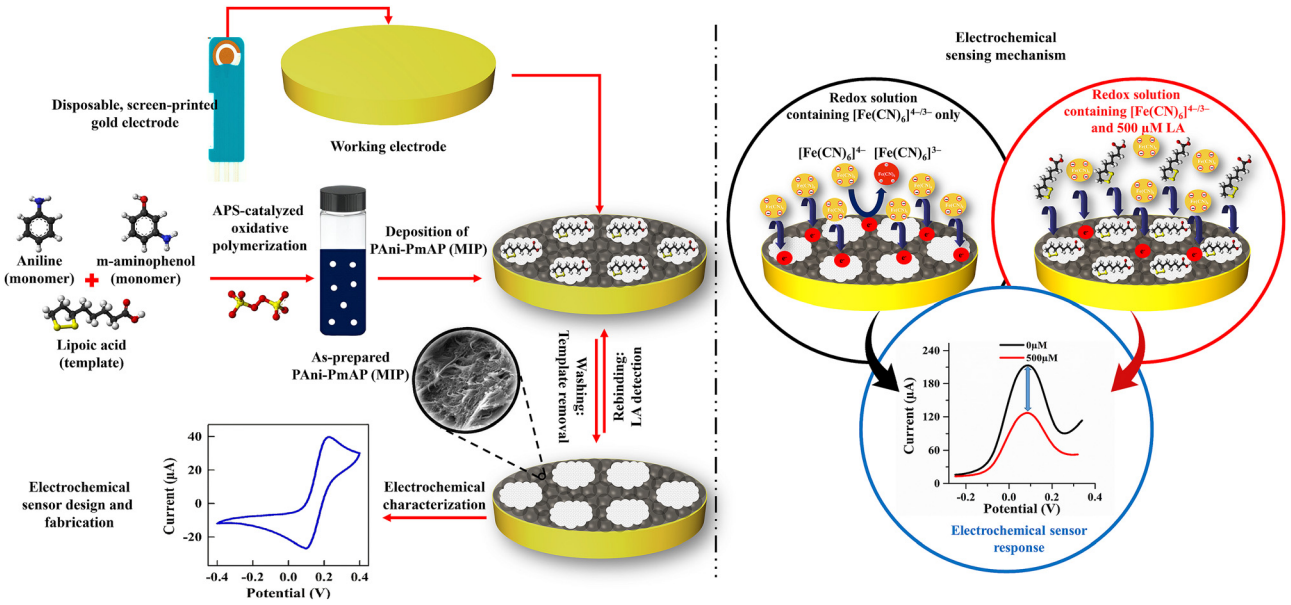

Fig. 1 (left) Schematic illustration of the synthesis and fabrication of the PAni–PmAP MIP on a disposable screen-printed gold electrode (SPGE). (right) Proposed mechanism of lipoic acid (LA) sensing: (black circle) In the absence of LA, the MIP sensor exhibits a high peak current in $[Fe(CN)_6]^{4-/3-}$ owing to unhindered access of redox species to the electrode surface. (red circle) Following exposure to 500 μM LA, selective binding at the imprinted sites restricts probe diffusion, reducing the current response. (blue circle) DPV profiles of the MIP sensor recorded before and after LA addition, demonstrating the signal suppression associated with analyte binding.

© 2025 The Author(s). Published by the Royal Society of Chemistry

Open Access Article. Published on 29 September 2025. Downloaded on 4/28/2026 6:53:28 PM.
This article is licensed under a Creative Commons Attribution-NonCommercial 3.0 Unported Licence.

under ambient conditions, with black coloration indicating successful polymer formation. The resulting MIP was collected by centrifugation at 4000 rpm for 5 minutes, washed three times with 10 mL of deionized water, and dried overnight in an oven at 60 °C. A non-imprinted polymer (NIP) was synthesized using the same procedure but without the addition of LA. A schematic of the synthesis process is presented in Fig. 1, along with the LA detection mechanism.

2.2. Sensor fabrication

To fabricate electrochemical sensors, 1 mg mL^{-1} suspensions of both MIP and NIP were prepared by dispersing the polymers in a 1% w/w polystyrene (PS) solution in tetrahydrofuran (THF), followed by 30 minutes of sonication. Screen-printed gold electrodes (SPGEs; ItalSens Gold, PalmSens BV, The Netherlands) were cleaned with ethanol and deionized water before modification. A 2 μL aliquot of the polymer suspension was drop-cast onto the working electrode area (3 mm diameter; 7.07 mm^2 surface area) and allowed to dry under ambient conditions for 30 minutes. To remove residual template molecules, the coated electrodes were rinsed 3–5 times with 0.01 M NaOH solution before electrochemical measurements. Additional experimental details on analytical and electrochemical characterization, sensor measurements, and the collection, pretreatment, and analysis of human serum samples are provided in the SI Experimental section.

3. Results and discussion

3.1. Analytical characterization

The FTIR spectra of MIP, NIP, and LA (Fig. 2a and b) provide insight into the structural features and successful imprinting of

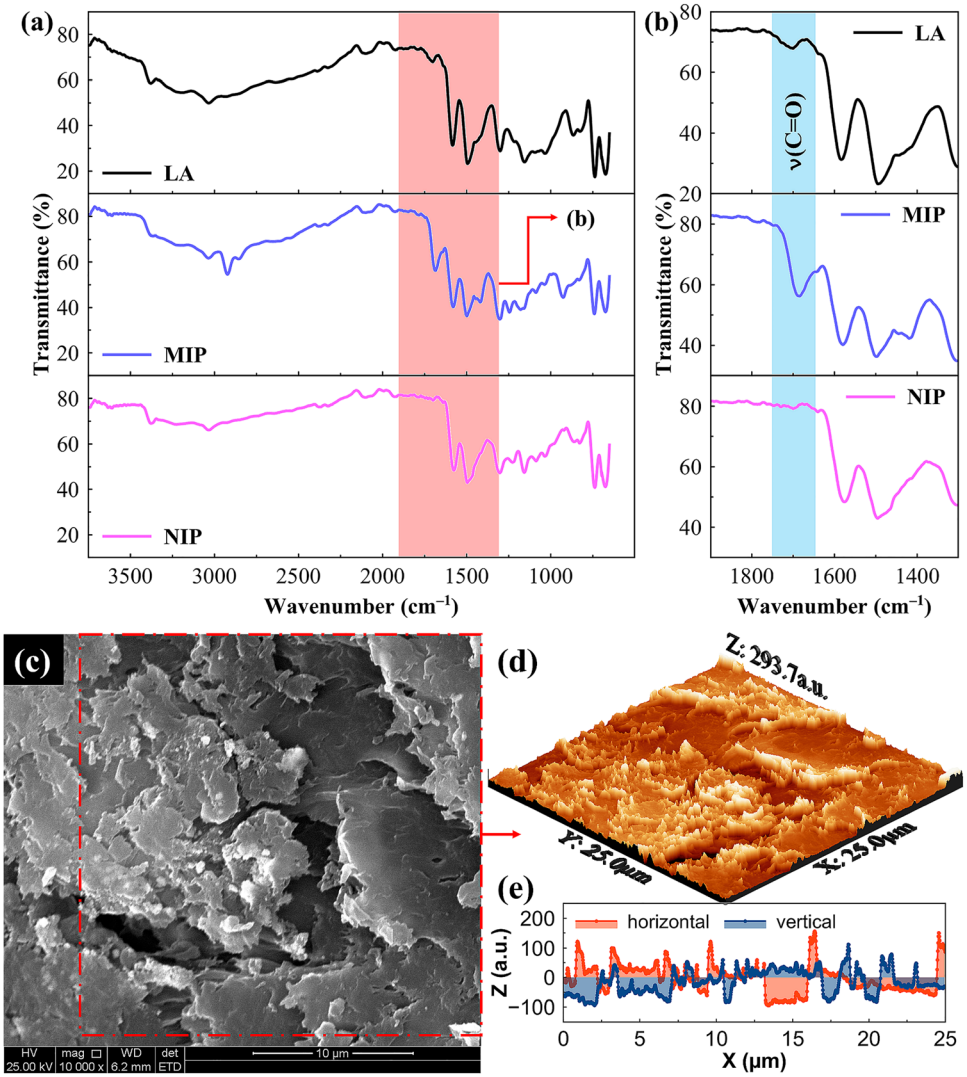

Fig. 2 Structural and morphological characterization. (a) FTIR spectra of PAni–PmAP copolymers (MIP and NIP), and lipoic acid (LA). (b) Enlarged fingerprint region highlighting the ν(C=O) peak shifts. Surface morphology of PAni–PmAP films: (c) SEM micrograph of the copolymer at 10 000× magnification (scale bar: 10 μm); (d) corresponding 3D surface topology; (e) surface height profiles extracted along the horizontal and vertical centerlines of (d).

Open Access Article. Published on 29 September 2025. Downloaded on 4/28/2026 6:53:28 PM.
This article is licensed under a Creative Commons Attribution-NonCommercial 3.0 Unported Licence.

the polymer matrix. As shown in Fig. 2a, both MIP and NIP display characteristic peaks of the poly(aniline-*co*-*m*-aminophenol) backbone, including C=N stretching at 1492 cm^{-1}, C–N stretching at 1299 cm^{-1}, C–H in-plane bending at 1157 cm^{-1}, and C–H out-of-plane bending at 739 cm^{-1}, consistent with literature values for aromatic amines and substituted aniline derivatives.[28,29] The broad absorption band in the 3376–3000 cm^{-1} range corresponds to overlapping N–H and O–H stretching vibrations, suggesting the presence of intermolecular hydrogen bonding within the copolymer network.[30] Importantly, the MIP spectrum shows additional weak absorption bands at 2925 cm^{-1}, 1690 cm^{-1}, and 1415 cm^{-1}, attributed to aliphatic C–H stretching, carbonyl C=O stretching, and symmetric C–O stretching, respectively.[31,32] These bands are absent in NIP, indicating that they arise from residual LA entrapped during the polymerization process (Fig. 2b). Their presence in MIP but not NIP confirms successful template incorporation and supports the creation of selective recognition sites. Hence, the spectral differences between MIP and NIP, despite having identical monomer compositions, reflect the specific molecular imprinting of LA and validate its interaction with the functional monomers during synthesis.

3.2. Surface analysis

The SEM micrographs display the surface morphology of the selective PAni–PmAP copolymer (MIP) (Fig. S1 and Fig. 2c–e). The lower magnification SEM images (500–5000×) establish overall coating uniformity and the general porous structure (Fig. S1), whereas the highest magnification (10 000×) allows for the visualization of finer morphological details and potential cavity-like features (Fig. 2c). The polymer demonstrates good surface uniformity, with minimal macroscopic defects. Notably, the dark regions observed in the micrographs correspond to porous features and cavity-like structures, likely representing imprinted sites formed by the removal of template LA molecules. These features are essential for selective target recognition. Further surface characterization using WSxM-processed[33] SEM data provides enhanced topographical insights (Fig. 2d and e). The pseudo-3D renderings confirm rough and porous morphology (Fig. 2d), attributed to the growth of MIP nanostructures and imprinting-induced surface heterogeneity.

The calculated root-mean-square roughness (R_{rms}) of 45.79 nm reflects the nanoscale texture of the surface, which is advantageous for increasing the electroactive area and facilitating analyte diffusion. The height distribution and lateral/vertical surface profiles (Fig. 2e) corroborate the existence of well-distributed surface features and a reasonably uniform morphology. Moreover, the surface kurtosis (S_{sk}) value of 3.7 indicates a leptokurtic distribution,[34] suggesting a balanced surface profile with enhanced surface contact area, favorable for consistent and efficient electrochemical interactions. These morphological traits validate the effectiveness of the electropolymerization and imprinting strategy in producing a structurally and functionally optimized MIP layer.[34,35]

3.3. Electrochemical characterization

EIS was applied to elucidate the interfacial properties of bare, NIP-, and MIP-modified SPGEs. The Nyquist plots and corresponding fits (Fig. 3a–c) in combination with the equivalent circuit models (Fig. S2) provide quantitative insight, while the Bode magnitude and phase spectra (Fig. 3d and e) reveal the

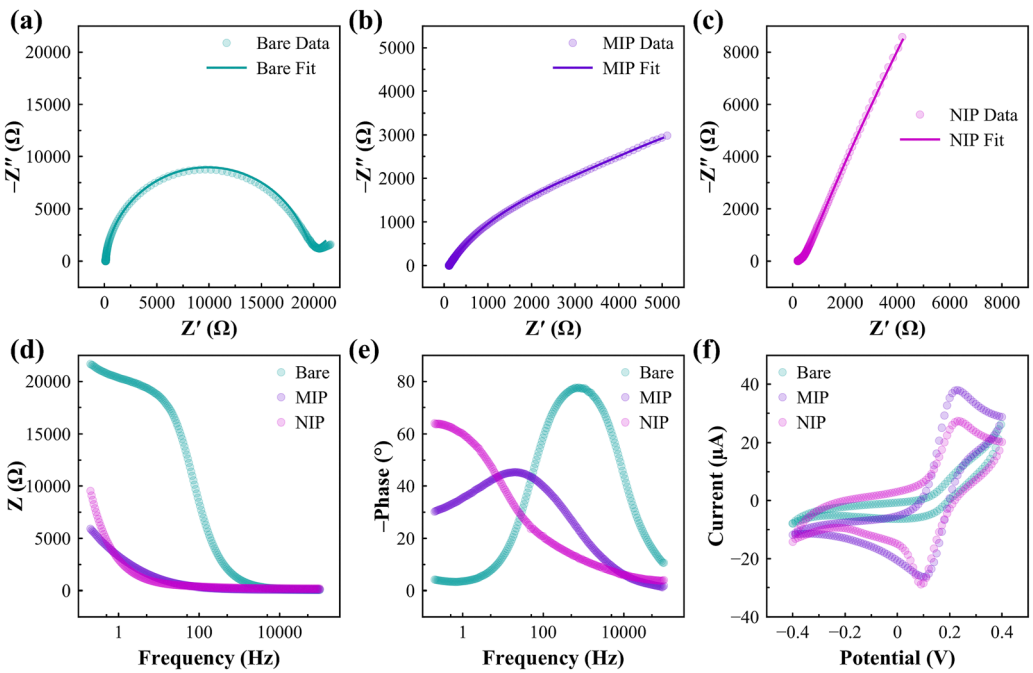

Fig. 3 Electrochemical characterization of the sensors: (a)–(c) Nyquist plots of (a) the bare, (b) MIP-, and (c) NIP-modified electrodes; (d) Bode magnitude plots; and (e) Bode phase angle plots of the bare, MIP-, and NIP-modified electrodes in a standard redox solution, with 2.5 mM $[Fe(CN)_6]^{3-/4-}$ and 0.05 M KCl in phosphate buffer (pH 7.4) at 25 °C. (f) CV scans of the bare, MIP-, and NIP-modified electrodes in a standard redox solution.

© 2025 The Author(s). Published by the Royal Society of Chemistry

Open Access Article. Published on 29 September 2025. Downloaded on 4/28/2026 6:53:28 PM.
This article is licensed under a Creative Commons Attribution-NonCommercial 3.0 Unported Licence.

dynamic relaxation processes across frequencies. The bare SPGE exhibited the largest charge transfer resistance (R_{ct} ≈ 19 kΩ; error = 0.342%; χ^2 = 0.0006), consistent with the large semicircle diameter in the Nyquist space (Fig. 3a) and the high low-frequency plateau of the Bode magnitude (Fig. 3d). Its phase spectrum showed a broad, low-frequency maximum (~80°), typical of sluggish electron transfer coupled with diffusion control (Fig. 3e). This response was best described by a simple Randles circuit with a Warburg element (Fig. S2, bare), confirming that interfacial charge transfer and semi-infinite diffusion dominate the bare electrode behavior.

The MIP electrode showed an intermediate R_{ct} of 4.7 kΩ (error = 3.5%; χ^2 = 0.00004) (Fig. 3b), reflecting improved conductivity compared with the bare electrode but partial blocking relative to NIP due to the presence of imprinted recognition cavities. In the Bode magnitude spectrum, the MIP trace lay between bare and NIP electrodes. Its phase response revealed a single, broad relaxation peak shifted to intermediate frequencies. This broadened phase feature, supported by the fitted CPE exponent values (Fig. S2, MIP), indicates a distributed interfacial process arising from the heterogeneity of the recognition cavities and their impact on local charge transfer and capacitance.[36–38] The MIP circuit (Fig. S2, MIP) included a CPE–*R* branch in parallel with a finite-length Warburg element, capturing the coupling between charge transfer and analyte diffusion through imprinted cavities.[36,37]

Modification with the NIP copolymer drastically lowered R_{ct} to 434 Ω (error ≈ 1%; χ^2 = 0.00006) (Fig. 3c), which confirmed enhanced interfacial conductivity and facilitated electron transport due to the high conductivity of the polymer backbone.[39,40] In the Bode magnitude plot (Fig. 3d), the NIP electrode showed the lowest overall impedance at low frequencies. Importantly, its phase spectrum contained two distinct relaxation features (Fig. 3e): a high-frequency shoulder linked to fast charge transfer through the polymer film, and a lower-frequency peak associated with hindered diffusion across the dense, non-specific polymer layer. This duality necessitated a more complex equivalent circuit (Fig. S2, NIP), including two parallel R-CPE branches and a Warburg element, consistent with two overlapping interfacial processes: conductive polymer pathways and restricted diffusion.[41,42] These findings highlight a clear progression in electrode behavior: (i) the bare SPGE is dominated by high charge transfer resistance and diffusion, (ii) the MIP-modified SPGE balances conductivity with selective molecular recognition, producing a broadened, intermediate-frequency relaxation and a coupled interfacial/diffusion process, and (iii) the NIP-modified SPGE promotes facile electron transfer but introduces a dense film that impedes diffusion, requiring two distinct time constants in the equivalent circuit.

The electrochemical behavior of the bare and modified electrodes (MIP and NIP) was evaluated using CV in a standard redox solution, as shown in Fig. 3f. The bare SPGE, characterized by high interfacial resistance and a negligible faradaic response, showed no measurable change in current upon the addition of LA and was therefore not included in the analytical calibration plots. Modification of the SPGE surface with PAni–PmAP resulted in a marked enhancement of the redox response compared to the bare electrode. This behavior arises from the redox-active nature of the PAni–PmAP backbone, which supports surface-confined faradaic processes, enhancing charge transfer and ion accessibility.[43] The anodic peak current (I_{pa}) increased from 27.34 μA for NIP to 38.02 μA for the MIP

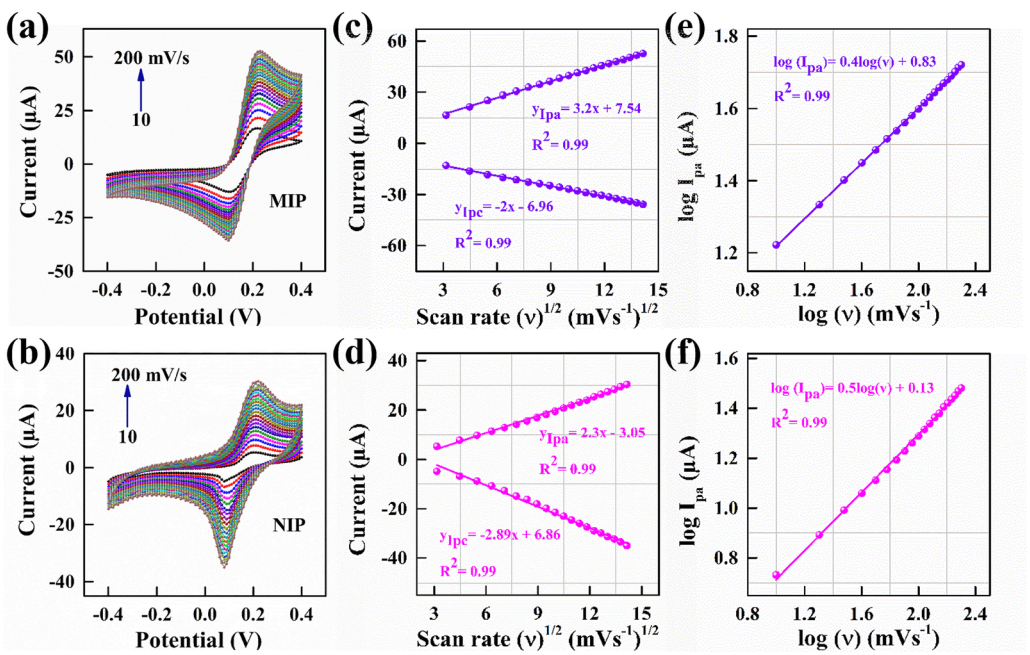

Fig. 4 Effect of scan rate on electrochemical response: (a) and (b) CV scans of MIP and NIP sensors at scan rates of 10–200 mV s^{-1} in a standard redox solution containing 2.5 mM $[Fe(CN)_6]^{4-/3-}$ and 0.05 M KCl in PBS (pH 7.4) at 25 °C. (c) and (d) The corresponding linear regression plots of anodic (I_{pa}) and cathodic (I_{pc}) peak currents *vs.* the square root of scan rate, and (e) and (f) log–log plots: log(I_{pa}) *vs.* log(ν) for the MIP and NIP sensors, respectively.

Open Access Article. Published on 29 September 2025. Downloaded on 4/28/2026 6:53:28 PM. This article is licensed under a Creative Commons Attribution-NonCommercial 3.0 Unported Licence.

electrodes, which reflected improved electron transfer, attributed to the enhanced conductivity, electroactive surface area, and accessible redox-active sites introduced by the polymeric coatings. The superior response of the MIP compared to the NIP further suggests the presence of binding sites, which facilitate more effective interaction with the redox species.

3.4. Effect of scan rate

The effect of scan rate (10–200 mV s^{-1}) on the electrochemical response of the modified electrodes was investigated using cyclic voltammetry (CV). Both MIP and NIP sensors exhibited a proportional increase in anodic peak current (I_{pa}) and a corresponding cathodic shift in the reduction peak (I_{pc}) with increasing scan rates (Fig. 4a and b), demonstrating that the redox process is influenced by the applied potential sweep. To elucidate the charge transfer mechanism, peak currents (I_{pa} and I_{pc}) were plotted against both the scan rate (ν) (Fig. S3) and the square root of the scan rate ($\sqrt{\nu}$) (Fig. 4c and d).[44,45] The excellent linearity observed in the I_p *vs.* $\sqrt{\nu}$ plots ($R^2 \approx 0.99$ for both MIP and NIP) confirms that the redox process is predominantly diffusion-controlled at the electrode–electrolyte interface.[46–48] The corresponding linear regression equations further substantiate this kinetic behavior. Additionally, log–log plots of I_{pa} *vs.* scan rate ($\log \nu$) (Fig. 4e and f) yielded slopes of 0.40 for MIP and 0.50 for NIP, aligning closely with theoretical values for diffusion-limited processes. These results validate that electron transfer at both modified surfaces occurs *via* diffusion-controlled mechanisms, though slight variations in slope suggest minor contributions from adsorption or surface interactions in the imprinted matrix.

3.5. Electrochemical properties

To quantitatively assess the electrochemical properties, the electroactive surface area (A) and the heterogeneous electron transfer rate constant (K^0) were calculated. The electroactive area was determined using the Randles–Ševčík equation (eqn (1)):

$$m = 2.69 \times 10^5 n^{3/2} A D^{1/2} C \quad (1)$$

where m is the slope of the I_{pa} *vs.* $\nu^{1/2}$ calibration plot (Fig. 4), n is the number of electrons transferred, A is the electroactive area, C is the concentration of the redox species, D is the diffusion coefficient, and ν is the scan rate.[49] The calculated electroactive areas were 1.95×10^{-2} cm^2 for the bare electrode, increasing to 4.00×10^{-2} cm^2 and 5.57×10^{-2} cm^2 for NIP and MIP, respectively. This notable increase confirms that the polymer layers significantly enhance the accessible surface for redox activity.

The heterogeneous electron transfer rate constant (K^0) was estimated using the following equation (eqn (2)):[50]

$$K^0 = RT/R_{ct}ACF^2 \quad (2)$$

where R_{ct} is the charge transfer resistance obtained from EIS, R is the gas constant, T is the temperature, and F is Faraday's constant. The K^0 values were found to be 1.76×10^{-4} cm s^{-1} for the bare electrode, increasing to 6.13×10^{-3} cm s^{-1} for NIP and 4.05×10^{-4} cm s^{-1} for MIP. These values fall within the expected range for polymer-modified electrodes probed with $[Fe(CN)_6]^{4-/3-}$, where conductive NIP films typically exhibit faster kinetics, while the presence of imprinted cavities introduces interfacial heterogeneity and lowers the apparent rate constant. These findings are consistent with the EIS data and confirm that imprinting enhances electrode surface area and molecular recognition at the expense of interfacial charge transfer kinetics.

3.6. Sensor measurements

CV was performed at a fixed scan rate of 100 mV s^{-1} to evaluate the response of the modified sensors across increasing LA concentrations (0–500 μM). As shown in Fig. S4a, b (SI), a progressive decrease in anodic peak current (I_{pa}) was observed with rising LA levels. This inverse trend suggests effective binding of LA at the electrode surface, which impedes electron transfer and alters the redox activity. A comparative analysis between the MIP and NIP sensors revealed markedly improved performance for the MIP sensor. The MIP demonstrated strong linearity between I_{pa} and LA concentration, with a coefficient of determination (R^2) of 0.97 (Fig. S4c, SI), outperforming the NIP sensor (R^2 = 0.93; Fig. S4d, SI). This higher linearity reflects the enhanced specificity and affinity of the imprinted polymer matrix for LA. The MIP sensor exhibited 43% greater sensitivity, calculated at 0.020 μA μM^{-1}, across a linear dynamic range of 0–500 μM. In contrast, the NIP sensor showed a reduced sensitivity of 0.014 μA μM^{-1}. These findings validate the enhanced recognition ability of the MIP sensor, which arises from the presence of selective molecular cavities formed during imprinting. These cavities enable specific binding interactions with LA, contributing to the sensor's high selectivity and improved analytical performance.

To further validate the electrochemical performance of the fabricated sensors, DPV measurements were carried out over a broad concentration range of LA (0–500 μM). DPV is a sensitive technique known for its high signal resolution and accuracy in quantifying electroactive analytes, particularly in complex matrices.[51,52] The resulting DPV curves (Fig. 5a and b) exhibit a consistent decline in peak current with increasing LA concentration, mirroring the trend observed in CV studies and confirming effective LA interaction with the polymer-modified electrode surfaces. Calibration plots (Fig. 5c) demonstrate linear current responses for both MIP and NIP sensors, with the MIP sensor showing 71% higher sensitivity compared to the NIP sensor. This superiority is consistent across techniques: analysis of the CV data (Fig. S4, SI) shows that the MIP sensitivity is 43% higher than NIP (0.020 *vs.* 0.014 μA μM^{-1}), while DPV shows a 71% advantage (0.144 *vs.* 0.084 μA μM^{-1}) (Fig. 5c). The significantly higher absolute sensitivity of DPV underscores its selection as the primary analytical method due to its superior resolution and minimized capacitive contributions.

Furthermore, the sensitivity in terms of current density per concentration (μA cm^{-2} μM^{-1}) was determined from the slope of the calibration curves (Fig. 5d), while LOD and LOQ were calculated using the standard regression approach: LOD = $3.3\sigma/S$; and LOQ = $10\sigma/S$;[51,52] where σ is the standard deviation of the

© 2025 The Author(s). Published by the Royal Society of Chemistry

Open Access Article. Published on 29 September 2025. Downloaded on 4/28/2026 6:53:28 PM.
This article is licensed under a Creative Commons Attribution-NonCommercial 3.0 Unported Licence.

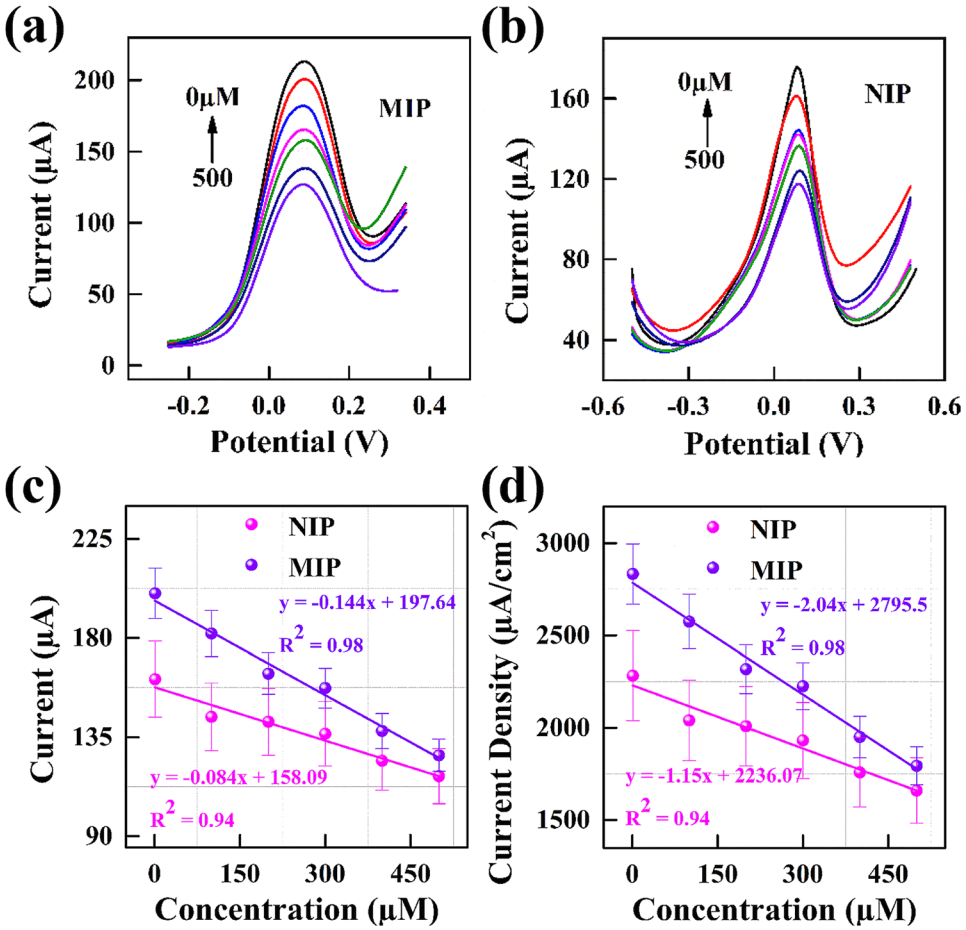

Fig. 5 DPV scans of (a) MIP and (b) NIP sensors at varying LA concentrations (0–500 μM) in a standard redox solution containing 2.5 mM $[Fe(CN)_6]^{3-/4-}$ and 0.05 M KCl in phosphate buffer (pH 7.4) at 25 °C with a scan rate of 100 mV s^{-1}. (c) Calibration plots of current response *vs.* LA concentration, and (d) current density *vs.* LA concentration for the MIP and NIP sensors.

blank signal (*y*-intercept of the calibration curve) and *S* is the sensitivity (slope of the calibration curve). Again, the MIP sensor exhibited superior analytical performance, with a high sensitivity of 2.04 μA cm^{-2} $μM^{-1}$, a low LOD of 189 nM, and an LOQ of 573 nM. The linearity was excellent across the tested concentration range, with a correlation coefficient (R^2) of 0.98, highlighting the sensor's robustness and precision at low analyte concentrations. On the contrary, the NIP sensor demonstrated lower sensitivity and less favorable detection limits, reaffirming the enhanced selectivity and electrochemical efficiency of the MIP sensor. These results are consistent with the EIS data, which exhibited that the NIP electrode exhibited high Warburg impedance and distinct dual relaxation, confirming the hindered mass transport through its compact non-selective film. By contrast, the MIP electrode displays a finite diffusion component coupled with charge transfer, reflected in its single broad relaxation. This behavior indicates that the imprinted cavities act as structured diffusion pathways that preserve accessibility while conferring molecular selectivity.

3.7. Sensing mechanism

The electrochemical behavior of MIP and NIP sensors, studied using CV in a $[Fe(CN)_6]^{3-/4-}$ redox system, indicates a diffusion-controlled redox process, as confirmed by the linear relationship between peak current and the square root of scan rate (Fig. 4).[53] The redox probe undergoes surface electron transfer reactions, and its access to the electrode determines the observed current response. Upon exposure to LA, a concentration-dependent decrease in peak current is observed in both the CV (Fig. S4) and DPV (Fig. 5) profiles. This decline is attributed to the binding of LA molecules within the imprinted cavities of the MIP, which physically obstructs diffusion of the redox probe to the electrode surface, thereby reducing the charge transfer rate.[54] The effect is more pronounced in MIP due to its specific recognition sites, whereas NIP lacks such selective interactions and exhibits a less significant current change. This selective recognition mechanism is analogous to antigen–antibody binding, where analyte capture impedes redox probe accessibility. Fig. 1 (right panel) schematically illustrates this concept, contrasting the unhindered redox process in the absence of LA with the diffusion-blocking effect upon LA binding.

3.8. Cross-sensitivity and selectivity analysis

Selectivity is a critical parameter for sensor performance in complex biological environments such as serum. DPV results

Open Access Article. Published on 29 September 2025. Downloaded on 4/28/2026 6:53:28 PM. This article is licensed under a Creative Commons Attribution-NonCommercial 3.0 Unported Licence.

(Fig. 5) confirmed the superior sensitivity of the MIP sensor compared to the NIP, justifying its use in cross-selectivity evaluations. This enhanced response is attributed to the presence of molecularly imprinted cavities that enable selective binding of LA, thereby reducing non-specific interactions. Selectivity measurement was performed using DPV in the presence of biorelevant compounds, such as cholesterol and cholic acid, across concentrations ranging from 1 to 500 μM, and the results were compared with lipoic acid. The MIP sensor showed a sensitivity of 0.144 μA μM^{-1} for LA, significantly exceeding its responses to cholesterol (0.034 μA μM^{-1}) and cholic acid (0.016 μA μM^{-1}), as shown in Fig. 6a and b. This clear difference reinforces the specificity of the MIP sensor and highlights its potential for accurate LA detection in complex biological samples. To further assess cross-sensitivity, the MIP sensor was tested against common biomolecular interferents including urea, uric acid, spermine, guanine, and glutamine. As shown in Fig. 6c, the MIP exhibited the highest response to LA, while responses to other analytes remained below 40% relative to LA, indicating strong molecular discrimination.

3.9. Analysis of human serum

Electrochemical detection of LA in complex biological fluids such as human serum poses considerable challenges due to the presence of potential interfering species. To evaluate the practical applicability of the fabricated MIP sensor, both unspiked and LA-spiked (100 μM) serum samples were analyzed. Following collection, the serum samples underwent a pre-treatment protocol involving dilution, centrifugation, and filtration (0.22 μm) to remove proteins and other macromolecules (SI: Experimental section). This step ensures the removal of biomacromolecules and protein-bound LA and enables the quantification of the free (unbound) fraction of LA, which is the pharmacologically active form most relevant for assessing therapeutic efficacy and potential toxicity. It is important because the molecularly imprinted cavities of the sensor are designed for the specific recognition of this free LA molecule. A schematic overview of the analysis protocol is shown in Fig. 7a.

The sensor exhibited a clear and measurable response in both sample types (Fig. 7b and c), demonstrating its functionality in real-world biological matrices. Recovery analysis was performed using five independent serum samples spiked with a known concentration of LA. The percentage recovery was calculated using the formula:[55]

$$\text{Recovery}\,(\%) = \frac{C_{\text{total}} - C_{\text{initial}}}{C_{\text{spiked}}} \times 100 \qquad (3)$$

The MIP sensor achieved a mean recovery of 102 ± 7.07%, confirming its high accuracy and reliability in detecting LA amidst potentially interfering serum constituents. These results highlight the sensor's suitability for point-of-care (POC) diagnostics, particularly in monitoring LA-related pathophysiological conditions such as NELL-1 MN and renal dysfunction.

3.10. Solvent and chemical stability

The sensor's operational stability and chemical stability of the MIP layer in the solvent after repeated exposures were evaluated over five consecutive days by monitoring its CV response toward 500 μM LA. As shown in Fig. 7d and e, the MIP sensor retained 85% of its initial response after five days of repeated measurements, indicating excellent durability. The robust PAni–PmAP imprinted layer maintained electrochemical performance with minimal degradation, underscoring the sensor's resilience under prolonged usage. In summary, the PAni–PmAP-based MIP sensor demonstrates high selectivity, sensitivity, and stability. These findings establish a practical platform for accurate, rapid, and sensitive LA monitoring, offering potential for early diagnosis and continuous management of kidney disorders in point-of-care settings.

3.11. Batch-to-batch reproducibility

The reproducibility of the sensor fabrication process was assessed by characterizing independently prepared electrodes (n = 2). As illustrated in Fig. S5, the electrochemical response of these sensors showed a high degree of consistency. The anodic peak currents for the $[Fe(CN)_6]^{3-/4-}$ redox probe clustered closely around a mean value of 35.0 μA, with a relative standard deviation (RSD) of 11.8%. This level of reproducibility is highly competitive for laboratory-scale, hand-cast electrochemical

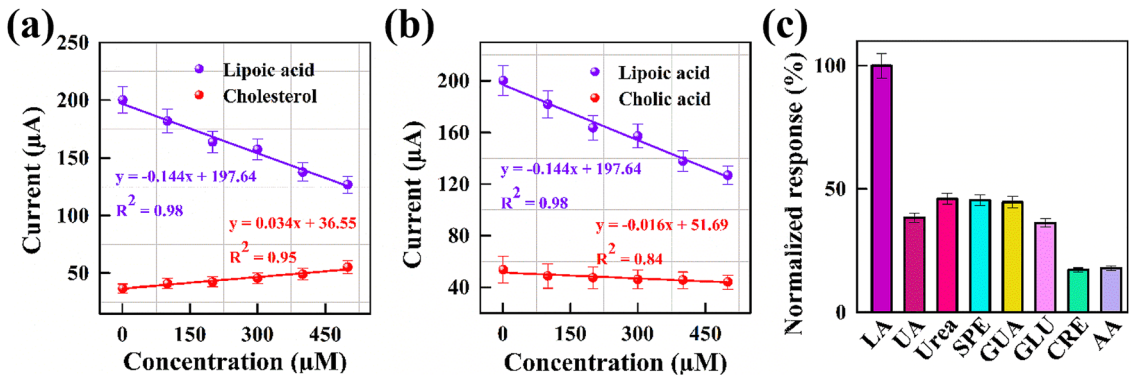

Fig. 6 Cross-sensitivity and selectivity analysis: calibration plots for the MIP sensor's response across 1–500 μM concentrations of (a) cholesterol and (b) cholic acid in a standard redox solution compared to the same concentration range of lipoic acid. (c) Normalized response of the MIP sensor upon exposure to different biomolecular analytes in a standard redox solution.

© 2025 The Author(s). Published by the Royal Society of Chemistry

Open Access Article. Published on 29 September 2025. Downloaded on 4/28/2026 6:53:28 PM.
This article is licensed under a Creative Commons Attribution-NonCommercial 3.0 Unported Licence.

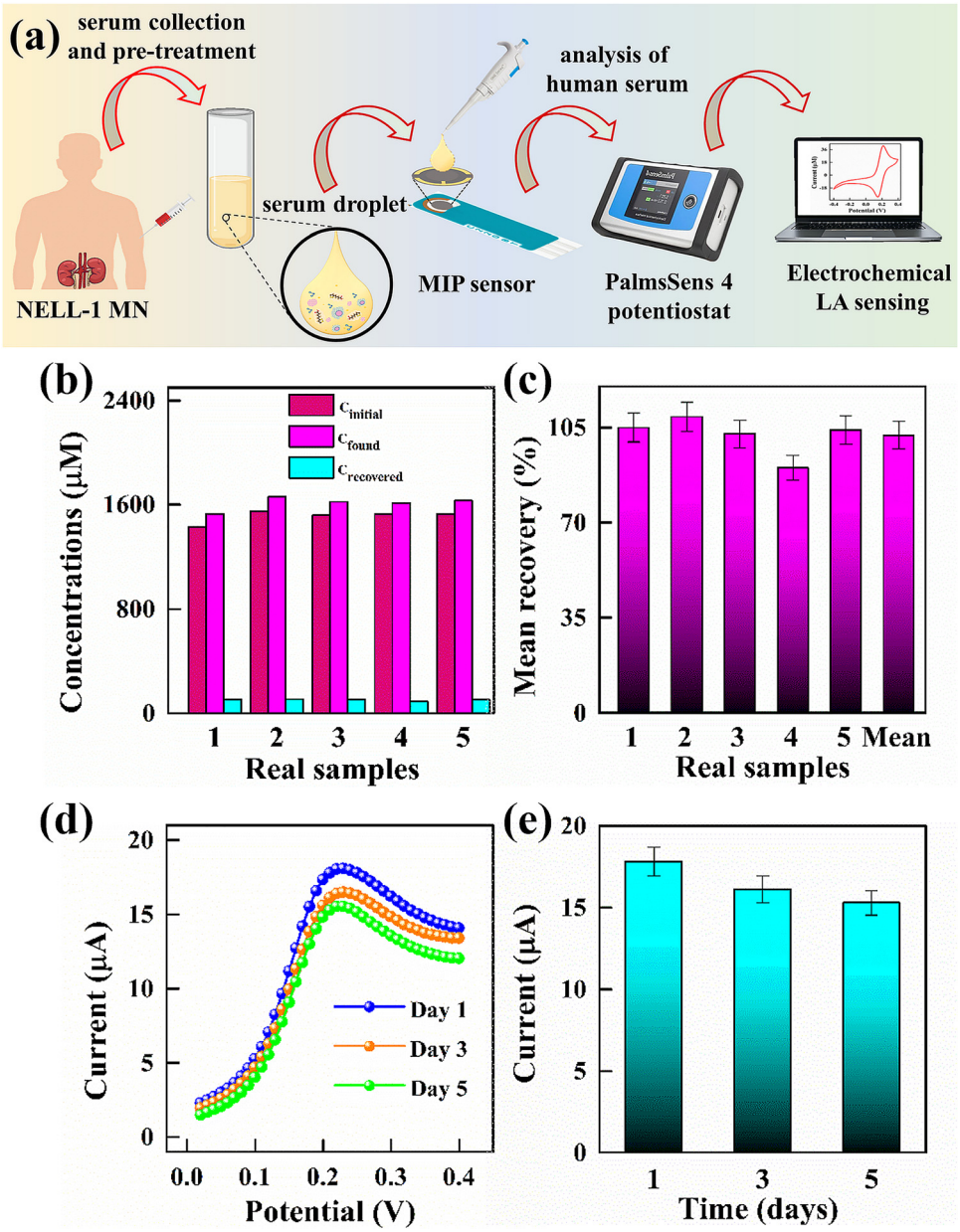

Fig. 7 Real-time analysis of lipoic acid (LA) in human serum samples is presented. (a) A schematic illustrating the design of the disposable and sensitive sensor for LA detection. (b) Actual and spiked serum samples from five different individuals are analyzed, and (c) the percent recovery of 100 μM spiked LA is shown, demonstrating the sensor's accuracy. For stability analysis, (d) cyclic voltammetry (CV) scans and (e) the corresponding current responses of the molecularly imprinted polymer (MIP) sensor toward 500 μM LA are recorded over five consecutive days of continuous electrochemical measurements.

sensors and underscores the robustness of the electrophysicization and drop-casting protocol. The low RSD value confirms that the procedure yields functionally equivalent sensor surfaces with minimal batch-to-batch variation, which is a critical prerequisite for any reliable analytical application.

3.12. Comparative analysis

The analytical performance of the PAni–PmAP-based MIP/SPGE sensor was compared with other reported methods for LA detection, as summarized in Table S1. The developed sensor demonstrates a competitive detection limit (0.189 μM), outperforming several electrochemical platforms, including those based on Pt and glassy carbon electrodes (GCEs),[56–58] and is comparable to more complex systems utilizing cobalt phthalocyanine/pyrolytic graphite[59] or boron-doped diamond electrodes.[60] The key advantage of our sensor lies in its unique combination of attributes: it achieves a high sensitivity (2.04 μA cm^{-2} $μM^{-1}$) while using a disposable, screen-printed gold electrode (SPGE) platform functionalized with a selective MIP layer. This design offers a practical, low-cost alternative to expensive HPLC-UV and HPLC-ECD methods without sacrificing performance.[61,62]

The developed MIP sensor, with 0.189 μM LOD, operates within a 1–500 μM range, well-suited for monitoring physiological and therapeutic levels of LA in serum, which typically

Open Access Article. Published on 29 September 2025. Downloaded on 4/28/2026 6:53:28 PM. This article is licensed under a Creative Commons Attribution-NonCommercial 3.0 Unported Licence.

range from 0.1–5 μM, depending on the supplementation.[9] While not as sensitive as centralized laboratory techniques,[61,62] the sensor offers a practical combination of selectivity, cost-effectiveness, and portability, making it ideal for point-of-care monitoring and frequent testing in outpatient or resource-limited settings. Its primary advantage lies in enabling decentralized management of chronic conditions requiring LA supplementation, where rapid, affordable measurements are more critical than ultra-sensitive detection.

4. Conclusion

In conclusion, this work presents a novel, low-cost, and disposable electrochemical sensor for the sensitive detection of lipoic acid (LA) in human serum, diagnosing the onset of NELL-1 membranous nephropathy (MN). The sensor employs a molecularly imprinted cross-linked PAni–PmAP copolymer, featuring a porous morphology with fine molecular cavities and low interfacial resistance, enabling enhanced electron transfer kinetics and high selectivity toward LA. Electrochemical characterization using CV, DPV, and EIS confirmed the sensor's outstanding performance. EIS measurements revealed efficient charge transfer with minimal electrode–electrolyte resistance and diffusion-controlled redox behavior. DPV demonstrated high sensitivity (2.04 μA cm^{-2} μM^{-1}) within a linear detection range of 0–500 μM, achieving low LOD and LOQ values of 189 nM and 573 nM, respectively, facilitating trace-level detection of LA in serum. The sensor exhibited excellent selectivity against common interferents and demonstrated robust operational stability, retaining 85% of its initial response over five days of repeated measurements. Importantly, the MIP sensor accurately quantified LA in spiked human serum samples, achieving a mean recovery of 102 ± 7.07%, underscoring its reliability for practical applications. Hence, the PAni–PmAP-based MIP sensor offers a promising and scalable platform for accurate, rapid, and sensitive detection of LA, demonstrating significant potential for clinical diagnostics and point-of-care monitoring in kidney-related disorders.

Author contributions

Kanwal Bashir performed the synthesis of materials, fabrication of devices, and electrochemical characterizations, designed the experiments, investigated sensor characteristics, and wrote the initial draft of the manuscript. Amir Habib and Imran Shakir performed characterization of the materials and validated the results. Tajamal Hussain provided resources, analyzed data, and suggested experiments. Adeel Afzal conceived the idea, acquired funding, provided resources, supervised the research work, managed the project, and revised the manuscript.

Conflicts of interest

The authors declare no conflict of interest.

Data availability

The data that support the findings of this study have been included in the supplementary information (SI). Supplementary information: experimental section, SEM images, equivalent circuit diagrams, I_{pa} *vs.* ν curves, CV scans, reproducibility results, a table of comparison, and corresponding references. See DOI: **https://doi.org/10.1039/d5ma00773a**.

Acknowledgements

Imran Shakir wishes to extend their sincere gratitude to the Deanship of Scientific Research at the Islamic University of Madinah (KSA) for the support provided to the post-publishing program. Adeel Afzal acknowledges with gratitude the partial financial support provided by the Royal Society of Chemistry Research Fund (Grant No. R24-1270738805). Adeel Afzal and Amir Habib gratefully acknowledge the Deanship of Scientific Research, University of Hafr Al Batin, and the Ministry of Education (KSA) for the partial provision of research facilities and support. Kanwal Bashir acknowledges the use of generative AI to improve the readability and language of the manuscript.

References

1 B. Salehi, Y. Berkay Yılmaz, G. Antika, T. Boyunegmez Tumer, M. Fawzi Mahomoodally, D. Lobine, M. Akram, M. Riaz, E. Capanoglu, F. Sharopov, N. Martins, W. C. Cho and J. Sharifi-Rad, *Biomolecules*, 2019, **9**, 356.
2 N. K. Andeen, V. L. Kung and R. S. Avasare, *Front. Nephrol.*, 2024, **4**, 1323432.
3 S. Zhou, F. Meng, S. Yue, H. Li, L. Zhang and T. Wang, *Clin. Kidney J.*, 2023, **16**, 756–759.
4 S. Sethi, *Clin. Kidney J.*, 2023, **16**, 442–446.
5 R. Nassar, S. A. Kadhem and M. Shakir, *Kans J. Med.*, 2023, **16**, 297–298.
6 G. K. Deepthi, Y. Sivudu, T. E. Divakar, D. P. Kumar and N. B. Murthy, *Int. J. Eng. Res. Technol.*, 2013, **2**, 4.
7 K. Borowczyk, M. Krawczyk, P. Kubalczyk and G. Chwatko, *Int. J. Eng. Res. Technol.*, 2015, **7**, 1785–1798.
8 M. Godlewska, A. Odachowska, M. Turkowicz and J. Karpinska, *J. Anal. Methods Chem.*, 2015, 535387.
9 G. Chwatko, M. Krawczyk, M. Iciek, A. Kamińska, A. Bilska-Wilkosz, B. Marcykiewicz and R. Głowacki, *Arabian J. Chem.*, 2019, **12**, 4878–4886.
10 H. Kataoka, N. Hirabayashi and M. Makita, *Methods in Enzymology*, Academic Press, 1997, vol. 279, pp. 166–176.
11 H. A. Saputra, *Monatsh. Chem.*, 2023, **154**, 1083–1100.
12 D. M. Stanković, E. Mehmeti and K. Kalcher, *Anal. Sci.*, 2016, **32**, 847–851.
13 G. K. Ziyatdinova, G. K. Budnikov and V. I. Pogorel'tsev, *J. Anal. Chem. (Transl. of Zh. Anal. Khim.)*, 2004, **59**, 288–290.
14 K. Charoenkitamorn, S. Chaiyo, O. Chailapakul and W. Siangproh, *Anal. Chim. Acta*, 2018, **1004**, 22–31.
15 G. Ziyatdinova and L. Gimadutdinova, *Sensors*, 2021, **21**, 7639.

© 2025 The Author(s). Published by the Royal Society of Chemistry

Open Access Article. Published on 29 September 2025. Downloaded on 4/28/2026 6:53:28 PM. This article is licensed under a Creative Commons Attribution-NonCommercial 3.0 Unported Licence.

16 Ö. Güngör, B. Kiliç, T. Seren KARASÜRMELİ, İ. Özcan and S. Köytepe, *Measurement*, 2021, **182**, 109752.
17 S. Lu, K. Zhang, Y. Liu, X. Zhan and R. Savari, *Environ. Res.*, 2024, **245**, 117369.
18 S. Ramanavicius and A. Ramanavicius, *Polymers*, 2021, **13**, 49.
19 Y. Pan, J. Zhang, X. Guo, Y. Li, L. Li and L. Pan, *Polymers*, 2024, **16**, 1597.
20 Á. Terán-Alcocer, F. Bravo-Plascencia, C. Cevallos-Morillo and A. Palma-Cando, *Nanomaterials*, 2021, **11**, 252.
21 S. Jadoun, U. Riaz and V. Budhiraja, *Med. Devices Sens.*, 2021, **4**, e10141.
22 Y. L. Mustafa, A. Keirouz and H. S. Leese, *J. Mater. Chem. B*, 2022, **10**, 7418–7449.
23 E. Kislenko, A. İncel, K. Gawlitza, B. Sellergren and K. Rurack, *J. Mater. Chem. B*, 2023, **11**, 10873–10882.
24 K. Narula, S. Rajpal, S. Bhakta, S. Kulanthaivel and P. Mishra, *J. Mater. Chem. B*, 2024, **12**, 5699–5710.
25 J. Kupai, M. Razali, S. Buyuktiryaki, R. Kecili and G. Szekely, *Polym. Chem.*, 2017, **8**, 666–673.
26 S. Ramanavičius, I. Morkvėnaitė-Vilkončienė, U. Samukaitė-Bubnienė, V. Ratautaitė, I. Plikusienė, R. Viter and A. Ramanavičius, *Sensors*, 2022, **22**, 1282.
27 R. W. Peeling and R. McNerney, *Expert Rev. Mol. Diagn.*, 2014, **14**, 525–534.
28 P. Rajakani and C. Vedhi, *Int. J. Ind. Chem.*, 2015, **6**, 247–259.
29 A. G. Mustafin, L. R. Latypova, A. N. Andriianova, I. N. Mullagaliev, S. M. Salikhov, R. B. Salikhov and G. S. Usmanova, *RSC Adv.*, 2021, **11**, 21006–21016.
30 G. Thenmozhi, P. Arockiasamy and R. J. Santhi, *Int. J. Electrochem.*, 2014, **2014**, 961617.
31 N. Ikuta, A. Tanaka, A. Otsubo, N. Ogawa, H. Yamamoto, T. Mizukami, S. Arai, M. Okuno, K. Terao and S. Matsugo, *Int. J. Mol. Sci.*, 2014, **15**, 20469–20485.
32 E. S. Dolinina, E. Y. Akimsheva and E. V. Parfenyuk, *Pharmaceutics*, 2020, **12**, 228.
33 I. Horcas, R. Fernández, J. M. Gómez-Rodríguez, J. Colchero, J. Gómez-Herrero and A. M. Baro, *Rev. Sci. Instrum.*, 2007, **78**, 013705.
34 A. Rehman, M. A. Ehsan, A. Afzal, A. Ali and N. Iqbal, *Analyst*, 2021, **146**, 3317–3327.
35 J. Paluszyński and W. Słówko, *J. Microsc.*, 2009, **233**, 10–17.
36 D. R. Franceschetti, J. R. Macdonald and R. P. Buck, *J. Electrochem. Soc.*, 1991, **138**, 1368.
37 V. V. Pototskaya and O. I. Gichan, *Int. J. Electrochem. Sci.*, 2019, **14**, 8195–8205.
38 B.-Y. Chang, *J. Electrochem. Sci. Technol.*, 2022, **13**, 479–485.
39 H. Zhang, L. Cheng, H. Shang, W. Zhang and A. Zhang, *Russ. J. Electrochem.*, 2021, **57**, 872–884.
40 W. D. Adane, B. S. Chandravanshi and M. Tessema, *Sens. Actuators, B*, 2023, **390**, 134023.
41 A. Ch. Lazanas and M. I. Prodromidis, *ACS Meas. Sci. Au*, 2023, **3**, 162–193.
42 W. Choi, H.-C. Shin, J. M. Kim, J.-Y. Choi and W.-S. Yoon, *J. Electrochem. Sci. Technol.*, 2020, **11**, 1–13.
43 J. Heinze, B. A. Frontana-Uribe and S. Ludwigs, *Chem. Rev.*, 2010, **110**, 4724–4771.
44 S. Athar, I. Zaman, A. Liaqat and A. Afzal, *ACS Appl. Polym. Mater.*, 2023, **5**, 10438–10445.
45 Z. Saddique, M. Saeed, M. Faheem, S. Z. Bajwa, A. Mujahid and A. Afzal, *Nanoscale Adv.*, 2024, **6**, 3644–3654.
46 H. Essousi, H. Barhoumi, S. Karastogianni and S. T. Girousi, *Electroanalysis*, 2020, **32**, 1546–1558.
47 E. Sharafi and S. Sadeghi, *New J. Chem.*, 2023, **47**, 500–514.
48 N. Tuan Anh, L. Minh Tung, L. Khanh Vinh, N. V. Quy, O. V. Hoang, N. Xuan Dinh and A.-T. Le, *Nanoscale Adv.*, 2024, **6**, 256–267.
49 M.-J. Song, J.-H. Kim, S.-K. Lee and D.-S. Lim, *Anal. Sci.*, 2011, **27**, 985–989.
50 Z. Saddique, M. Saeed and A. Afzal, *ACS Appl. Nano Mater.*, 2024, **7**, 13472–13480.
51 B. J. Privett, J. H. Shin and M. H. Schoenfisch, *Anal. Chem.*, 2010, **82**, 4723–4741.
52 S. Baluta, F. Meloni, K. Halicka, A. Szyszka, A. Zucca, M. Itria Pilo and J. Cabaj, *RSC Adv.*, 2022, **12**, 25342–25353.
53 A. M. Abdel-Aziz, H. H. Hassan and I. H. A. Badr, *ACS Omega*, 2022, **7**, 34127–34135.
54 N. Shahzad and A. Afzal, *Microchim. Acta*, 2025, **192**, 163.
55 M. Saeed, Z. Saddique, A. Mujahid and A. Afzal, *Biosens. Bioelectron.*, 2024, **247**, 115899.
56 M. Marin, C. Lete, B. N. Manolescu and S. Lupu, *J. Electroanal. Chem.*, 2014, **729**, 128–134.
57 O. Corduneanu, M. Garnett and A. M. O. Brett, *Anal. Lett.*, 2007, **40**, 1763–1778.
58 G. K. Ziyatdinova, L. V. Grigor'eva and G. K. Budnikov, *J. Anal. Chem.*, 2009, **64**, 185–188.
59 A. P. M. Ferreira, L. N. dos Santos Pereira, I. S. da Silva, S. M. C. N. Tanaka, A. A. Tanaka and L. Angnes, *Electroanalysis*, 2014, **26**, 2138–2144.
60 D. M. Stanković, E. Mehmeti and K. Kalcher, *Anal. Sci.*, 2016, **32**, 847–851.
61 G. Chwatko, P. Kubalczyk and E. Bald, *Curr. Anal. Chem.*, 2014, **10**, 320–325.
62 A. Khan, Z. Iqbal, D. G. Watson, A. Khan, I. Khan, N. Muhammad, S. Muhammad, H. A. Nasib, N. Iqbal, F. Rehman and M. Kashif, *J. Chromatogr. B*, 2011, **879**, 1725–1731.

© 2025 The Author(s). Published by the Royal Society of Chemistry